Supplementary Information (SI) for Journal of Materials Chemistry A.

Supporting Information

Synergistic Structural and Electronic Engineering for Boosted Oxygen Evolution Reaction on Nickel-Iron Hydroxide Nanocatalysts

Jilan Zeng,[ab] Siping Wang,[ab] Xinran Sun,[ab] Jiaqing Liu,[ab] Kai Lin,*[ab] Shiqiang Feng,*[c] Jiayi Chen,[ab] Sibo Wang [ab] and Xue Feng Lu *[ab]

[a] State Key Laboratory of Chemistry for NBC Hazards Protection, College of Chemistry, Fuzhou University, Fuzhou 350116, China.

[b] State Key Laboratory of Photocatalysis on Energy and Environment, College of Chemistry, Fuzhou University, Fuzhou 350116, P. R. China.

[c] Fujian Science & Technology Innovation Laboratory for Optoelectronic Information of China, Fuzhou 350108, P. R. China.

E-mail: kailin@fzu.edu.cn; fsqvictor@pku.edu.cn; luxf@fzu.edu.cn

Experimental Section

Chemicals. Nickel nitrate hexahydrate ($Ni(NO_3)_2\cdot 6H_2O$, AR), iron nitrate nonahydrate ($Fe(NO_3)_3\cdot 9H_2O$, AR), cobalt nitrate hexahydrate ($Co(NO_3)_2\cdot 6H_2O$, AR), manganese nitrate hexahydrate ($Mn(NO_3)_2\cdot 4H_2O$, AR), and chromium nitrate hexahydrate ($Cr(NO_3)_3\cdot 9H_2O$, AR) were purchased from Aladdin Co., Ltd (Shanghai, China). N-methyl-2-pyrrolidone (NMP), ethanol, and potassium hydroxide (KOH) were provided by Sinopharm Chemical Reagent Co., Ltd (Shanghai, China). Anhydrous ruthenium oxide (RuO_2) was purchased from Sinero Technology Co., Ltd (Suzhou, China). All aqueous solutions were prepared using ultrapure water (resistivity = 18.2 MΩ cm, Milli-Q water) throughout the whole experiment. All the reagents are used without any further purification.

Synthesis of $Ni_3Fe_1Co_1$-Gly solid sphere precursors. 87 mg $Ni(NO_3)_2\cdot 6H_2O$, 40 mg $Fe(NO_3)_3\cdot 9H_2O$, and 29 mg $Co(NO_3)_2\cdot 6H_2O$ were dissolved in a mixed solvent of 8 mL glycerol and 40 mL isopropanol (stirred at 800 r/min for 40 min) to form a uniform transparent solution. The as-prepared solution was then transferred to a 100 mL Teflon-lined stainless-steel autoclave and kept at 200 °C for 10 hours. The resulting precipitate was washed with ethanol 5 times (dried at 60 °C), and the product was labeled as $Ni_3Fe_1Co_1$-Gly (subscripts indicate the molar ratio of metal ions). The preparation method of Ni_4Fe_1-Gly was similar, except that the metal salts were adjusted to 116 mg $Ni(NO_3)_2\cdot 6H_2O$ and 40 mg $Fe(NO_3)_3\cdot 9H_2O$. Similar, $Ni_{3.5}Fe_1Co_{0.5}$-Gly: 101.5 mg $Ni(NO_3)_2\cdot 6H_2O$, 40 mg $Fe(NO_3)_3\cdot 9H_2O$, and 14.5 mg $Co(NO_3)_2\cdot 6H_2O$; $Ni_2Fe_1Co_2$-Gly: 58 mg $Ni(NO_3)_2\cdot 6H_2O$, 40 mg $Fe(NO_3)_3\cdot 9H_2O$, and 58 mg $Co(NO_3)_2\cdot 6H_2O$.

Synthesis of M-Gly (M = Ni, Fe, Co, Mn, Cr) solid sphere precursors. For Niglycerate, 145 mg $Ni(NO_3)_2\cdot 6H_2O$ and 7.5 mL of glycerol were dissolved into 52.5 mL of isopropanol, and then 1 mL of water was dropped into the solution, after stirring for 40 min at 800 rpm, the as-prepared solution was then transferred to a Teflon-lined stainless steel autoclave and kept at 200 °C for 10 hours. The resulting precipitate was washed with ethanol 5 times (dried at 60 °C), and the product was labeled as Ni-Gly. For Fe-glycerate, prepared similarly using 151 mg $Fe(NO_3)_3\cdot 9H_2O$, 8 mL glycerol, and 40 mL isopropanol, with hydrothermal treatment at 180 °C for 10 h. For Co-glycerate or Mn-Gly, synthesized analogously using either 175 mg $Co(NO_3)_2\cdot 6H_2O$ or 151 mg $Mn(NO_3)_2\cdot 4H_2O$, with a 6 h reaction time at 180°C. The preparation methods of NiCo-Gly, NiMn-Gly, and NiCr-Gly were similar, except that the metal salts were adjusted to 44 mg $Ni(NO_3)_2\cdot 6H_2O$ combined with either 44 mg $Co(NO_3)_2\cdot 6H_2O$ (for NiCo-Gly), 38 mg $Mn(NO_3)_2\cdot 4H_2O$ (for NiMn-Gly), or 60 mg $Cr(NO_3)_3\cdot 9H_2O$ (for NiCr-Gly).

Synthesis of $Ni_3Fe_1Co_1(OH)_x$ hollow spheres. The synthesis of $Ni_3Fe_1Co_1(OH)_x$ adopted a solvothermal-induced structural reconstruction strategy: 100 mg of $Ni_3Fe_1Co_1$-Gly was ultrasonically dispersed in 10 mL NMP, and 10 mL deionized water was added (stirred at 600 r/min for 30 min). The mixture was transferred to a 50 mL Teflon-lined stainless-steel autoclave and reacted at 160 °C for 16 hours. After the precipitate was washed with ethanol 5 times (dried at 60 °C), the product was labeled as $Ni_3Fe_1Co_1(OH)_x$ (subscripts indicate the molar ratio of metal ions). The preparation method of $Ni_3Fe_1Co_1(OH)_x$, $Ni_4Fe_1(OH)_x$ was the same, except that the precursor was replaced with Ni_4Fe_1-Gly. The preparation methods of $Ni_{3.5}Fe_1Co_{0.5}(OH)_x$ and $Ni_2Fe_1Co_2(OH)_x$ were identical, except that the precursors were replaced with the corresponding precursors ($Ni_{3.5}Fe_1Co_{0.5}$-Gly for $Ni_{3.5}Fe_1Co_{0.5}(OH)_x$ and $Ni_2Fe_1Co_2$-Gly for $Ni_2Fe_1Co_2(OH)_x$).

Material Characterization. X-ray diffraction (XRD) patterns are collected on a MiniFlex 600 instrument with Cu Kα1 irradiation (λ = 1.5406 Å). Field-emission scanning electron microscopy (FESEM) images are collected on a Hitachi SU 8010. Transmission electron microscopy (TEM) was tested on JEM-2100F, and an energy-dispersive spectroscopy (EDS) mapping transmission electron microscope was tested on Noran System 7. Inductively coupled plasma atomic emission spectrometry (ICP-AES) determines the metal content on a PerkinElmer Avio 200. X-ray photoelectron spectroscopy (XPS) analysis is performed on an ESCALAB 250Xi instrument with a monochromatized Al Kα line source. All the XPS signals are calibrated by reference to the C 1s peak. Raman spectra were measured with a Horiba-Jobin Yvon (LabRAM HR Evolution) Raman spectrometer equipped with 532 nm illumination lasers.

Electrochemical Measurements. All electrochemical measurements were performed using a CHI 760E electrochemical workstation (Shanghai, China) in a standard three-electrode system in O_2-saturated 1.0 M KOH electrolyte at room temperature. The Hg/HgO (1.0 M KOH) electrode and graphite rod are used as the reference and counter electrode, respectively, and a catalyst-coated carbon paper as the working electrode. In a typical preparation process of catalyst ink, the sample (8 mg) was dispersed in the mixture of ultrapure water (300 μL), ethanol (100 μL), and 5 wt.% Dupont Nafion solution (40 μL). And then, the above ink was ultrasonicated for 1 hour to achieve homogeneity. The dispersion (40 μl) was pipetted onto a piece of clean carbon paper (CP, 0.5 cm × 0.5 cm), which was subjected to overnight solvent evaporation in air. The mass loading of catalysts was 2.9 mg cm^{-2}.

The potentials are calibrated to a reversible hydrogen electrode (RHE) via the Nernst equation: E (V vs. RHE) = E (V vs. Hg/HgO) + 0.098 + 0.059 × pH. Before conducting any electrochemical tests, cyclic voltammetry (CV) was first performed at a scan rate of 5 mV s^{-1} for 20 cycles to stabilize the catalyst. The linear sweep voltammetry (LSV) scan rate is 5.0 mV s^{-1}. All LSV measurements were corrected for ohmic resistance (iR correction, 95%) using the automatic compensation function of the electrochemical workstation. The electrochemical impedance spectroscopy (EIS) measurement is carried out at different potentials with a frequency range from 10^{-2} Hz to 10^{5} Hz with an amplitude of 5 mV. The durability test is performed in 1.0 M KOH solution using chronoamperometry. The C_{dl} was determined with typical CV tests at various scan rates (10, 20, 30, 40, 50, 60 mV s^{-1}) in the non-faradic region (under a potential window of 1.05 ~ 1.15 V vs RHE). The C_{dl} was estimated by plotting the half of the difference between anodic current density and cathodic current density ($j_a - j_c$) at 1.10 V against the scan rate.

Turnover frequency (TOF) calculation. The TOF values were calculated as the number of oxygen molecules evolved per active site per second based on the following equation:

$$\mathrm{TOF} = \frac{j \times N_A}{4 \times \mathrm{m} \times F}$$

Where j (A cm^{-2}) is the current density at a given overpotential, N_A is the Avogadro constant (6.023×10^{23} mol^{-1}), m is the surface concentration of active sites or number of participating atoms in the catalyst material, and F is the Faraday constant (96485 C mol^{-1}).[1]

For the OER catalyzed by 3d transition metal-based electrocatalysts, integrating the area under the redox peak corresponding to the transformation from oxide/hydroxide to oxyhydroxide is the most appropriate and meaningful method to determine the surface concentration of active metal sites.[2-4] Combining the potential range of the redox peak and the results of Raman analysis (only the signal of Ni−O bonds was detected), the peak in the CV curve (Segment 20, Fig. 3b) can be confirmed that the main transformation is Ni^{2+}/Ni^{3+} transition.

For $Ni_3Fe_1Co_1(OH)_x$/CP-2.9 mg cm^{-2}:

Reduction peak area = 1.86 V mA cm^{-2}

Charge associated with MOOH formation = 1.86 V mA cm^{-2} × 0.25 cm^2 / 5 mV s^{-1}

= 0.093 A s

= 0.093 C

Charge of an electron =1.602 × 10^{-19} C

Hence,

Number of electrons transferred is = 0.093 C / 1.602 × 10^{-19} C

= 5.8 × 10^{17}

If the single-electron transfer process is assumed to participate in the formation of M-OOH species (as a simplified treatment), the number of electrons transferred during the reaction is exactly equal to the number of active sites.

Similarly, the number of active sites calculated for $Ni_4Fe_1(OH)_x$ is 3.2 × 10^{17}, $Ni_{3.5}Fe_1Co_{0.5}(OH)_x$ is 3.7×10^{17}, and $Ni_2Fe_1Co_2(OH)_x$ is 4.8×10^{17}.

For example, the TOF value at an overpotential of 250 mV for $Ni_3Fe_1Co_1(OH)_x$ is

$$\text{TOF} = 0.012\ \text{A} \times 6.023 \times 10^{23}\ \text{mol}^{-1} / (4 \times 96485\ \text{C mol}^{-1}\ (\text{or A s}) \times 5.8 \times 10^{17})$$

$$= 3.3 \times 10^{-2}\ \text{s}^{-1}$$

However, we acknowledge that assuming a universal single-electron transfer for all active sites to calculate the number of active sites is indeed a relatively crude treatment. Nevertheless, all NiFeCo-LDH samples in this study possess similar phase compositions, crystal structure characteristics, and redox behaviors. The consistent application of this single-electron transfer assumption across all tested samples ensures the reliability of the relative trend of catalytic activity reflected by the TOF values, which is also the core purpose of TOF calculation in this study.

In-situ Raman measurements. CP coated with the catalyst was used as the working electrode, with a platinum wire and an Ag/AgCl electrode serving as the counter and reference electrodes, respectively. These three electrodes were then mounted in the Raman cell, into which 1.0 M KOH electrolyte was injected. A laser wavelength of 532 nm was used. The electrochemical workstation was used to perform the chronoamperometry method, with set potentials (OCV, 1.30, 1.35, 1.40, 1.45, 1.50, 1.55, 1.60 V) and holding times. For each specific potential, a 200-second stabilization period was allowed to achieve steady-state electrode conditions before collecting Raman signals.

AEMWE Test. The anion exchange membrane electrolysis single cell consists of an anion exchange membrane (AEM, DQ-AEM045), electrodes, gas diffusion layer (GDL), bipolar plates with a flow distributor, and end plates. To avoid carbon corrosion under the high anodic potential conditions, we employed carbon paper as the cathodic GDL, while a more corrosion-resistant nickel foam was used as the anodic GDL. $Ni_3Fe_1Co_1(OH)_x$ and commercial Pt/C (20 wt.% Pt) were used as the anode and cathode, respectively. The catalyst loadings were controlled at 6.0 mg cm^{-2} for $Ni_3Fe_1Co_1(OH)_x$ and 0.1 mg_{Pt} cm^{-2} for Pt/C, calculated against the 5 cm × 5 cm active area of the membrane. The catalyst inks were prepared as follows:

For the anode, 300 mg $Ni_3Fe_1Co_1(OH)_x$ catalyst and 45 mg solid ionomer (PiperION-A TP-85) were dispersed in a mixed solvent of deionized water and isopropanol (volume ratio 1:9). For the cathode, Pt/C catalyst was dispersed in the same solvent system. Both inks were subjected to ultrasonic dispersion for 60 min to ensure homogeneous dispersion without agglomeration. Subsequently, the catalysts were sprayed (CHERSONIC, UAM4000-SS) onto both sides (with an active area of 5 cm × 5 cm) of the AEM, with process parameters configured: Spray length/width = 60.00 mm (covering the 5 cm × 5 cm active area with margin), spray height = 55.0 mm, single-pass spray width = 5.0 mm, Working speed = 8400 mm min^{-1}, rapid traverse speed = 3000 mm min^{-1}, Total spray passes = 90, single-pass duration = 5.6 s. The spraying process was conducted on a vacuum adsorption platform to fix the membrane and avoid wrinkling. The built-in 80°C heating pad of the spray equipment can remove the solvent during the spraying process, thereby preventing uneven distribution of the catalyst. After the spraying process is completed, the membrane electrode assembly with the deposited catalyst layers needs to be transferred to the hot press (ERRIFIC TOOLS, JYWFC-M) for further curing treatment. The assembled membrane electrode assembly used 30 wt.% KOH solution as the electrolyte, which flowed through both sides at a rate of 80 mL min^{-1} to maintain uniform ion transport and mitigate concentration polarization. The cell temperature is precisely controlled at 60 °C with an automatic temperature control device, and the system is stabilized at the target temperature for 30 min to ensure thermal equilibrium.

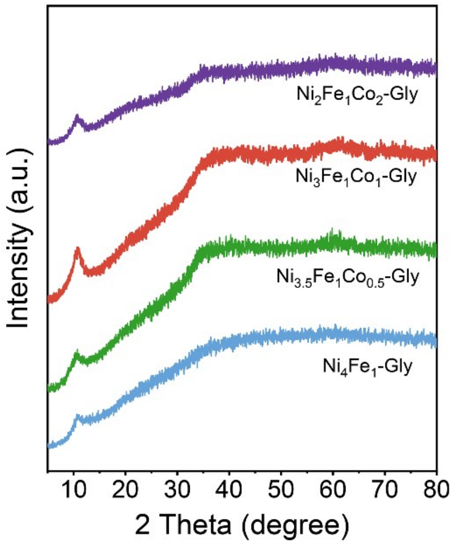

Fig. S1 XRD patterns of NiFeCo-Glys with different Co contents.

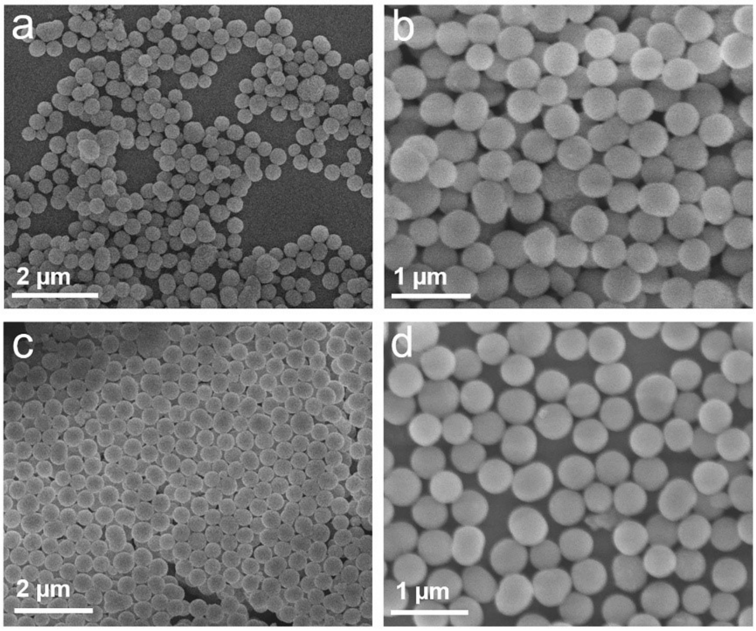

Fig. S2 FESEM images of NiFeCo-Glys with different Co contents.

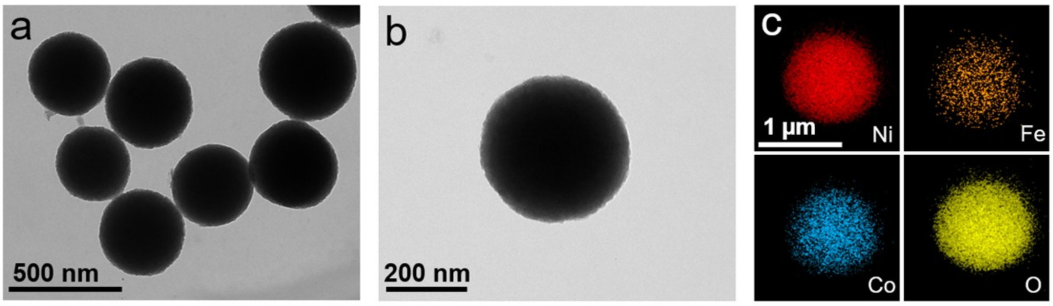

Fig. S3 (a, b) TEM and (c) EDS elemental mapping images of $Ni_3Fe_1Co_1$-Gly.

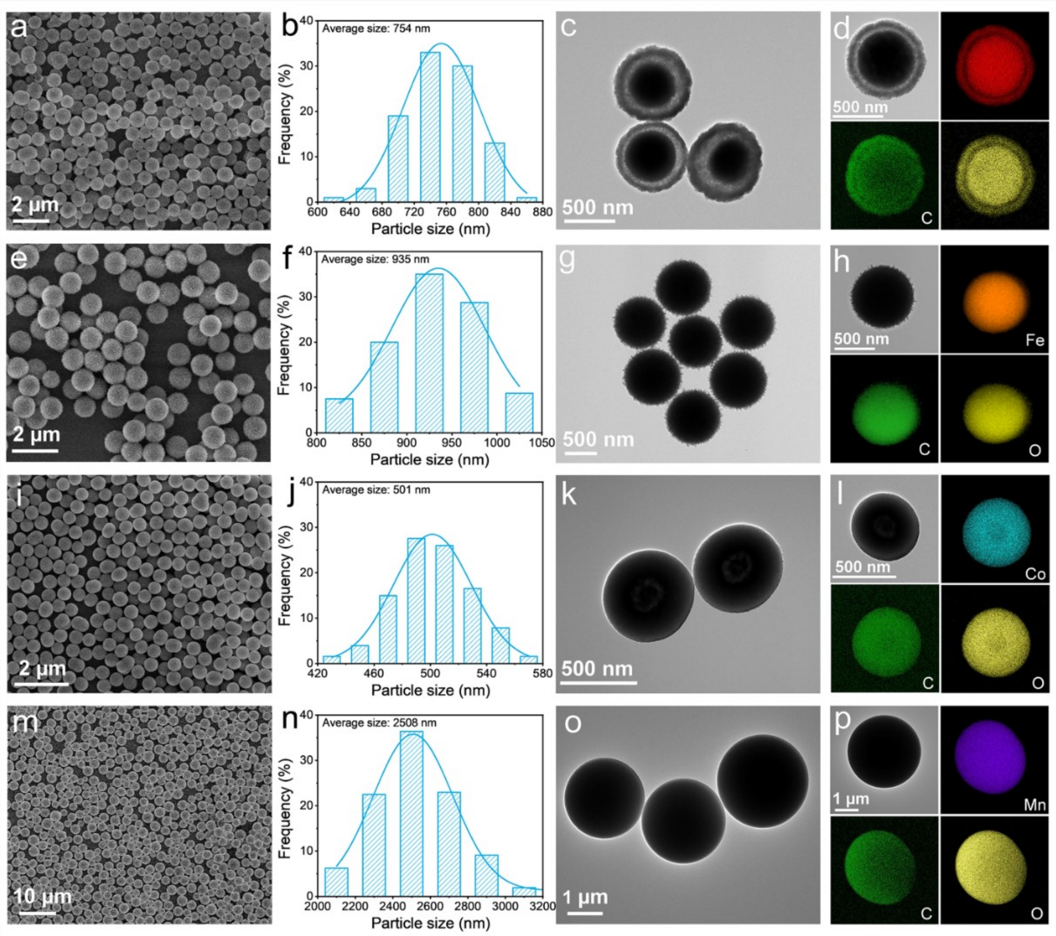

Fig. S4 FESEM images, particle size distribution histograms derived from FESEM images, TEM images, and EDS elemental mapping images of (a-d) Ni-Gly, (e-h) Fe-Gly, (i-l) Co-Gly, and (m-p) Mn-Gly, respectively.

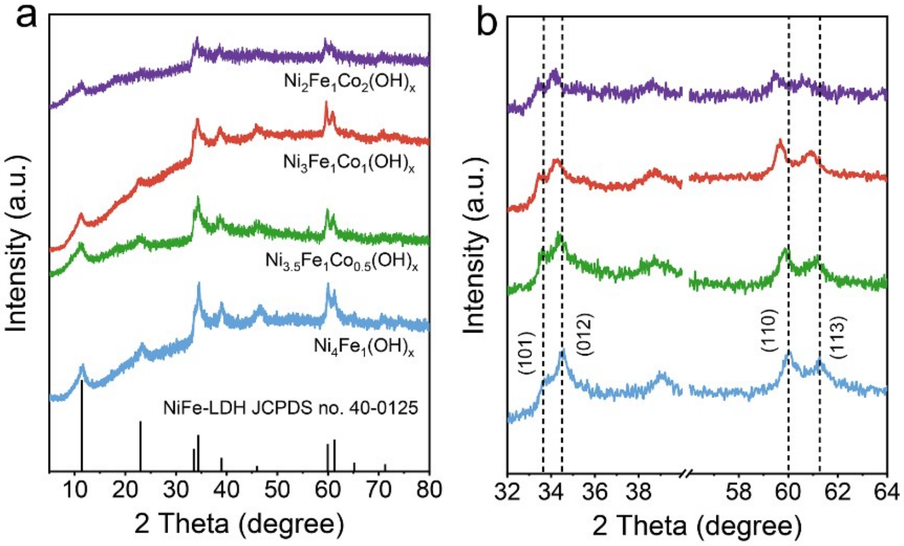

Fig. S5 (a) XRD patterns of NiFeCo-LDHs with different Co contents. (b) Partial enlargement of the XRD patterns highlights the gradual shift of peaks with increasing Co content, which indicates lattice distortion.

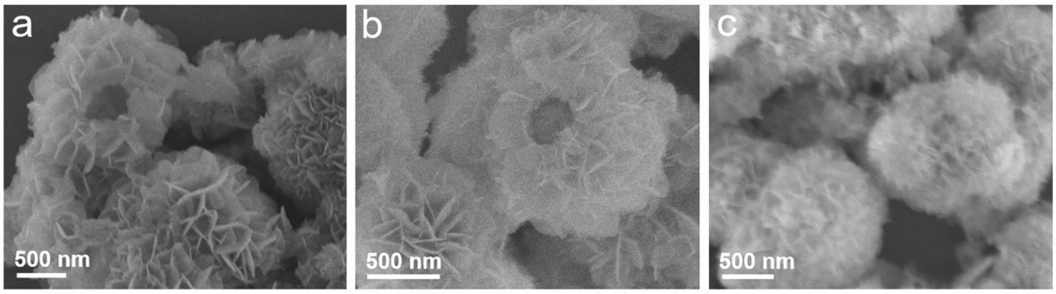

Fig. S6 FESEM images of (a) Ni_4Fe_1 $(OH)_x$, (b) $Ni_{3.5}Fe_1Co_{0.5}(OH)_x$, and (c) $Ni_2Fe_1Co_2(OH)_x$.

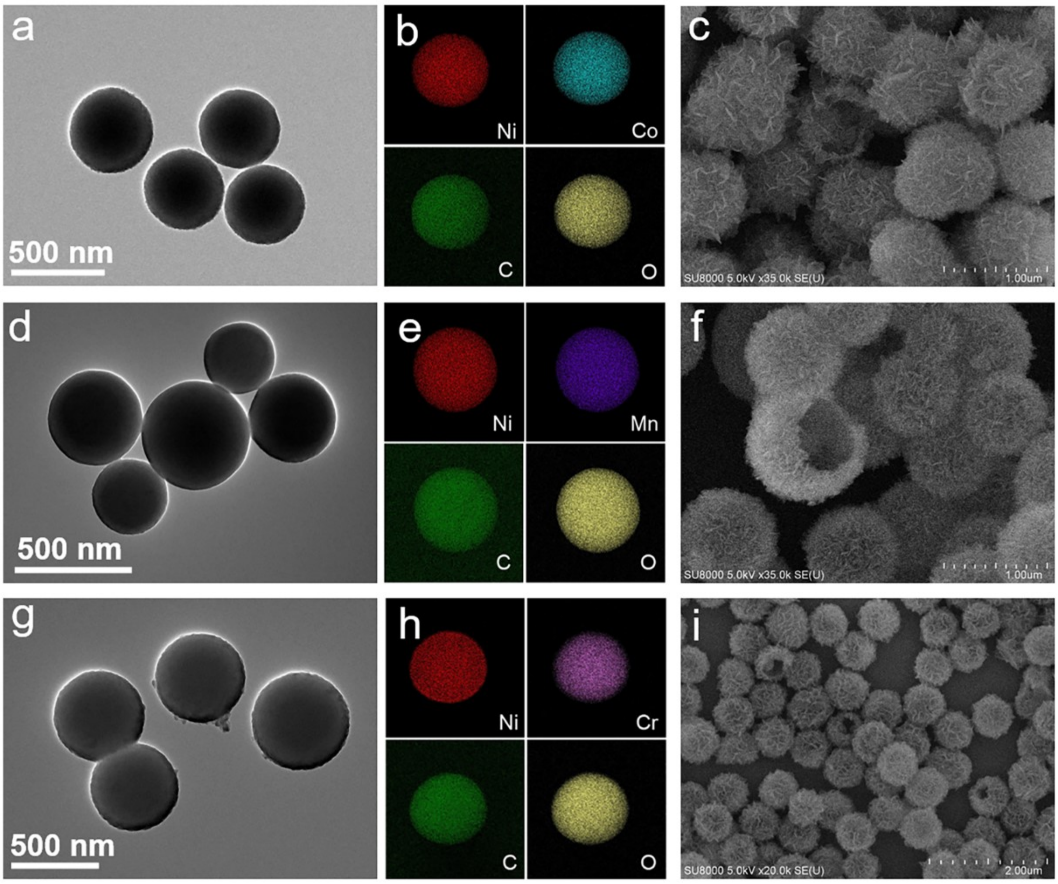

Fig. S7 TEM and EDS elemental mapping images of the (a, b) NiCo-Gly, (d, e) NiMn-Gly, and (g, h) NiCr-Gly precursors. (c, f, i) FESEM images of the corresponding hydrolysis products of the above precursors.

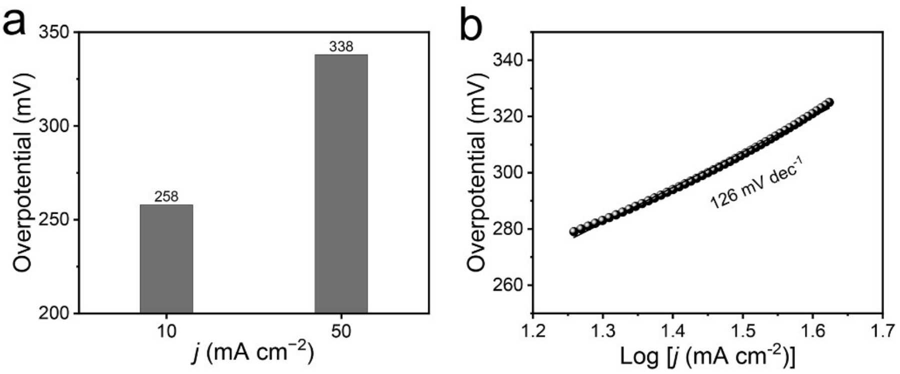

Fig. S8 (a) The overpotentials at 10 and 50 mA cm^{-2} and (b) Tafel solpe of RuO_2.

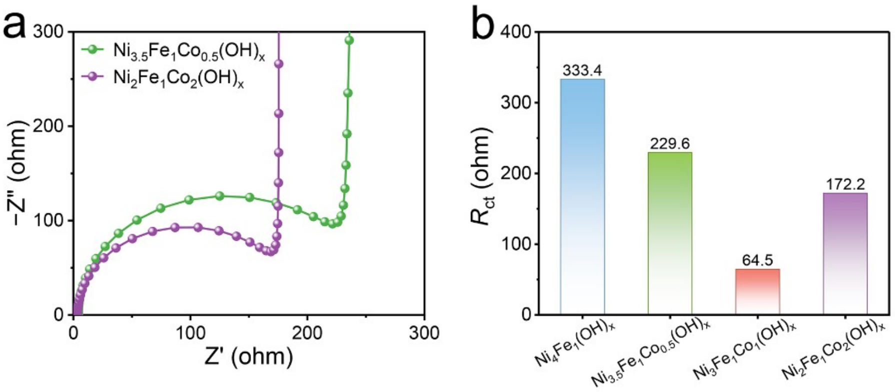

Fig. S9 (a) Nyquist plots of $Ni_{3.5}Fe_1Co_{0.5}(OH)_x$ and $Ni_2Fe_1Co_2(OH)_x$. (b) R_{ct} values.

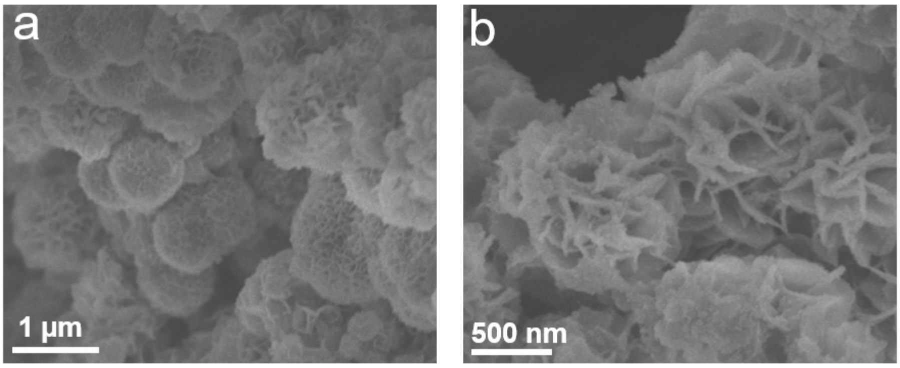

Fig. S10 (a, b) FESEM images of $Ni_3Fe_1Co_1(OH)_x$ after 100 h stability test.

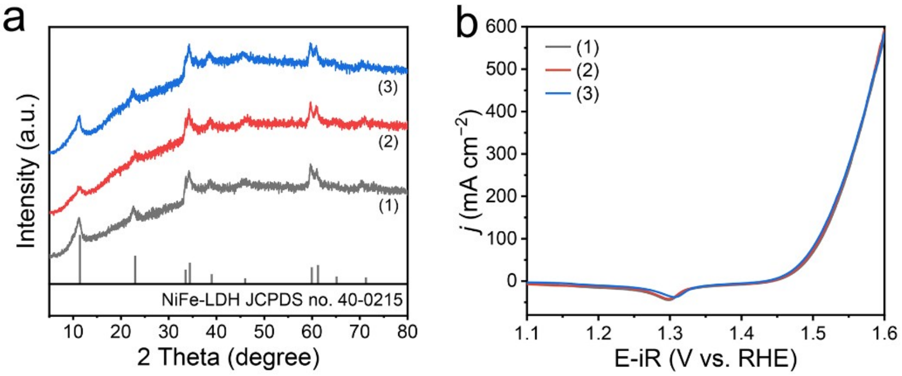

Fig. S11 (a) XRD patterns and (b) LSV curves of three batches of $Ni_3Fe_1Co_1(OH)_x$.

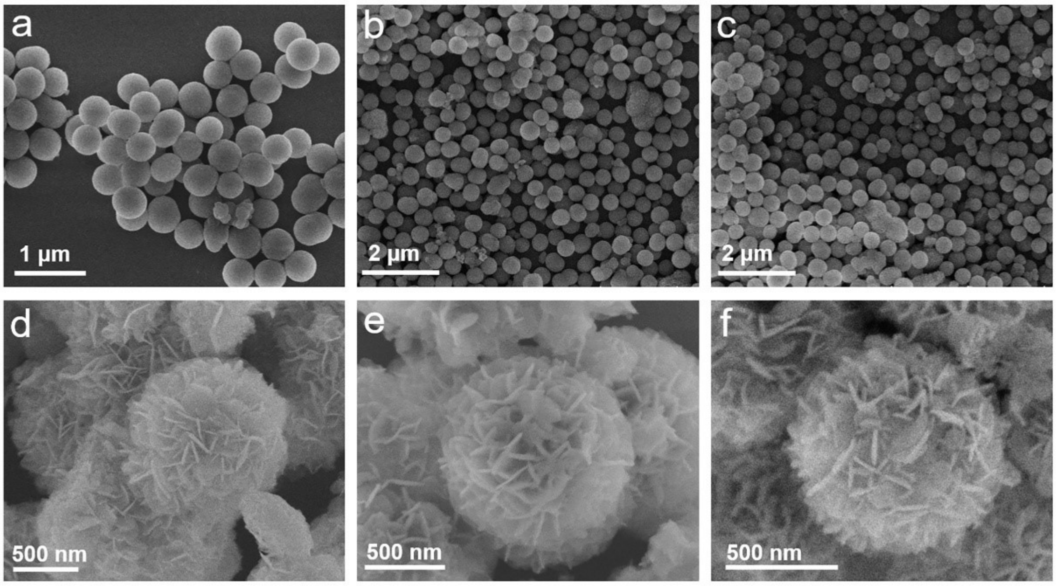

Fig. S12 FESEM images of three batches of (a-c) $Ni_3Fe_1Co_1$-Gly and (d-f) $Ni_3Fe_1Co_1(OH)_x$.

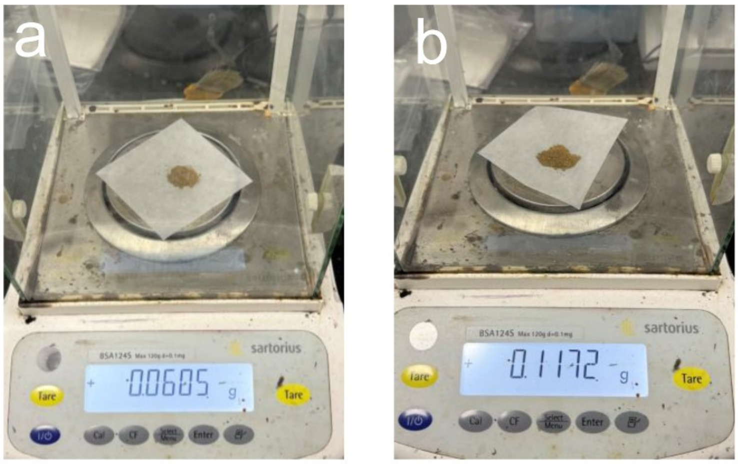

Fig. S13 Photographs of weighed laboratory-synthesized $Ni_3Fe_1Co_1(OH)_x$ products. (a) ~0.06 g product (standard batch: 0.1 g precursor/50 mL autoclave); (b) ~0.12 g product (2-fold scaled-up batch: 0.2 g precursor/100 mL autoclave), confirming preliminary synthetic scalability.

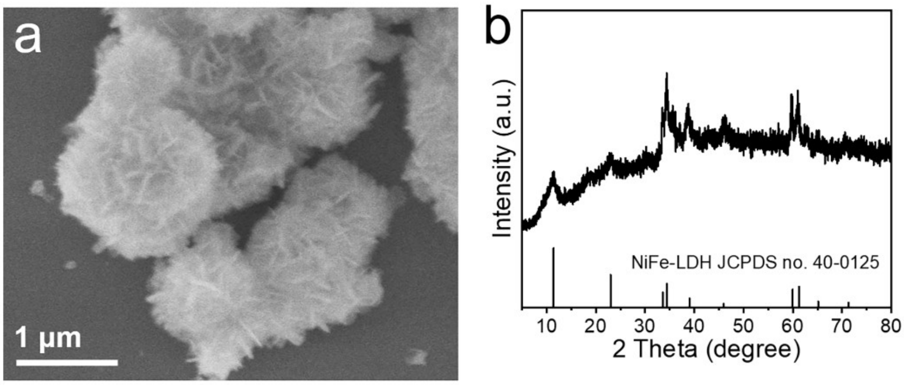

Fig. S14 (a) FESEM image and (b) XRD pattern of $Ni_3Fe_1Co_1(OH)_x$ from the 2-fold scaled-up batch.

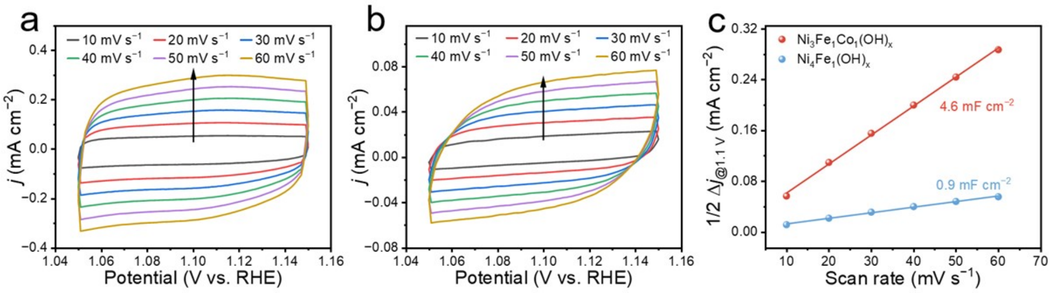

Fig. S15 CV curves of (a) $Ni_3Fe_1Co_1(OH)_x$ and (b) $Ni_4Fe_1(OH)_x$. (c) C_{dl} values of the two samples.

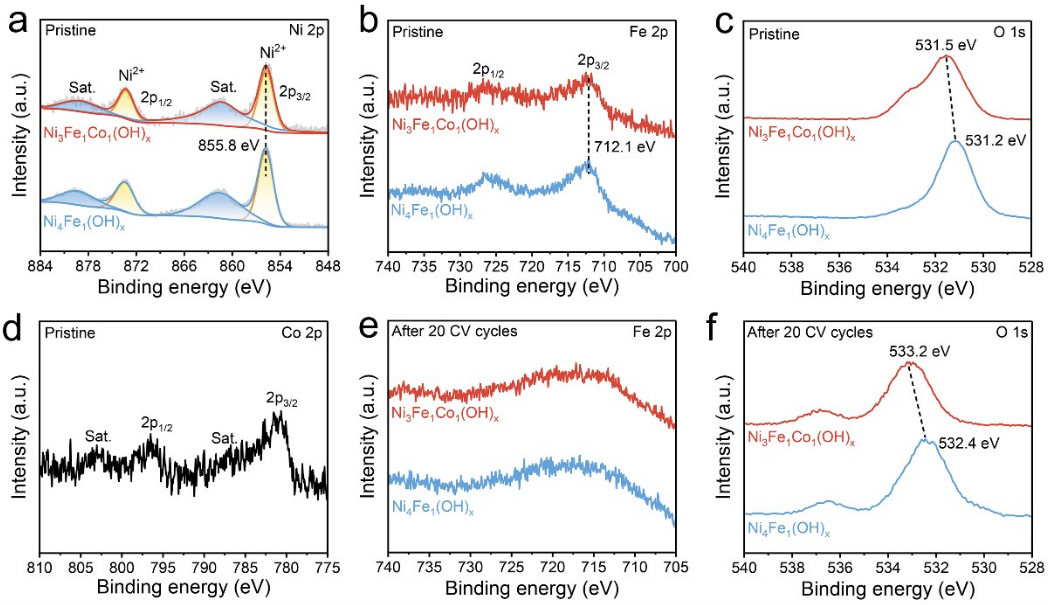

Fig. S16 (a-c) The Ni 2p, Fe 2p, and O 1s XPS spectra of two samples in their pristine state. (d) The Co 2p XPS spectrum of $Ni_3Fe_1Co_1(OH)_x$ in its pristine state. (e, f) Fe 2p and O 1s XPS spectra of two samples after 20 CV cycles.

Note: In the pristine state, the binding energy positions of Ni and Fe in the two samples are consistent (**Fig. S16a, b**), indicating that the Ni and Fe are in similar electronic environments. Notably, the O 1s peak shifts overall toward higher binding energies (**Fig. S16c**), a phenomenon that can be attributed to the oxidation of part of Co^{2+} to Co^{3+} during synthesis (corresponding reaction: $Co(OH)_2 + OH^- \rightarrow Co(OH)_3 + e^-$, $E = -0.17$ V) (**Fig. S16d**). After electrochemical activation, the XPS spectra of Fe in the two samples show similar characteristics (**Fig. S16e**); while the O 1s peak further shifts toward higher binding energies (**Fig. S16f**), a result confirming the formation of higher-valent $Ni^{3+\delta}$ species during the activation process.

Fig. S17 Digital photographs of (a) the spray-coating process, (b) $Ni_3Fe_1Co_1(OH)_x$ sprayed sprayed membrane electrode and (c) the AEMWE electrolysis apparatus for overall water splitting.

Table S1. The content of metal elements measured by ICP-OES.

Sample	Ni (wt.%)	Fe (wt.%)	Co (wt.%)	Atomic·ratio of Ni:Fe(:Co) (Normalized to Co)
$Ni_4Fe_1(OH)_x$	37.6	9.7	-	3.7:1.0
$Ni_{3.5}Fe_1Co_{0.5}(OH)_x$	32.7	9.8	4.9	6.7:2.1:1.0
$Ni_3Fe_1Co_1(OH)_x$	28.2	10.2	9.0	3.1:1.2:1.0
$Ni_2Fe_1Co_2(OH)_x$	18.0	9.6	17.1	1.0:0.6:1.0

Table S2. Comparison of the OER performance for different Ni-based catalysts.

Catalyst	η_{10} (mV)	Tafel slope (mV dec^{-1})	Reference
$Ni_3Fe_1Co_1(OH)_x$	218	52	This work
Ni(OH)S	250	77	5
NiFe(DMBD)	295	32	6
NiCoFe-HO@NiCo-LDH	278	50	7
FeCoNi-LDHs	269	42	8
FeNiBDC	239	75	9
G-FeNi-Co-ZIF-L/NF	248	50	10
$NiCo_2O_4$/NiCoFe-OH	235	65	11
NiFeW LDH	249	79	12
$Ni_{0.5}Fe_{0.5}$-THQ	272	48	13
NiCo-LDH@rGO	376	74	14
$Co_{0.4}Fe_{0.6}$ LDH/g-CN_x	280	29	15
Fe-doped $Ni(OH)_2$ nanosheets/NF	219	53	16
NiFeCo-LDH	249	42	17
Ni-Fe LDH hollow nanoprisms	280	50	18
Mo-doped NiFe (oxy) hydroxide	242	23	19
$Ni(CN)_2/NiSe_2$ Heterostructures	270	68	20
NiFeV-LDH	287	54	21
NiFe-LDH@La SNHPC	251	53	22
$NiMoO_4$	230	60	23
Ni–Fe alloy	265	40	24
P−NiFeOxHy	242	50	25
NiFeZn-LDH	240	19	26
$NiSe_2/FeSe_2$	230	28	27
$Cr_xMnFeNi$	255	29	28
NiOOH/MnFeOOH	261	38	29
NiFe_FA_NN	256	56	30

Table S3. The fitting data of R_s and R_{ct} for $Ni_3Fe_1Co_1(OH)_x$.

Potential (V vs. RHE)	R_s (ohm)	R_{ct} (ohm)
1.30	3.66	30.87
1.35	3.65	11.33
1.40	3.47	2.36
1.45	3.38	1.57
1.50	3.34	0.84
1.55	3.31	0.42
1.60	3.25	0.29

Note: R_s stands for solution resistance, and R_{ct} represents charge transfer resistance. As shown in the above table, $Ni_3Fe_1Co_1(OH)_x$ exhibits a smaller R_{ct} value, which confirms that the Co-substituted NiFe-LDH has superior charge transfer kinetics.

Table S4. The fitting data of R_s and R_{ct} for Ni_4Fe_1 $(OH)_x$.

Potential (V vs. RHE)	R_s (ohm)	R_{ct} (ohm)
1.30	4.34	259.7
1.35	4.33	180.2
1.40	4.38	129.3
1.45	4.39	3.7
1.50	4.25	2.22
1.55	4.11	1.74
1.60	4.13	1.47

Table S5. Metal element content in powders after three-electrode stability test.

Sample	Ni (wt.%)	Fe (wt.%)	Co (wt.%)	Atomic·ratio of Ni:Fe(:Co) (Normalized to Co)
$Ni_4Fe_1(OH)_x$	30.4	9.8	-	2.9:1.0
$Ni_3Fe_1Co_1(OH)_x$	25.8	9.7	8.1	3.2:1.3:1.0

Table S6. Performance comparison of different anode catalysts in AEMWE.

Anode	Voltage (V)@*j* (mA cm^{-2})	Temperature (°C)	Electrolyte	Reference
$Ni_3Fe_1Co_1(OH)_x$	1.79@1000	60	30 wt. %	This work
$Co_{2.8}$, $W_{3.8}$-NiFe LDH	1.86@1000	60	1.0 M KOH	31
Cr-NiFe-LDH	2.11@1000	40	1.0 M KOH	32
$SmNi_{0.02}Fe$-LDH	2@900	Room temperature	1.0 M KOH	33
NiFeCo-LDH	1.8@802	50	1.0 M KOH	34
$Ni/NiFeCo(OH)_x$	1.75@500	40	1.0 M KOH	35
$CoCrO_x$	2@500	60	1.0 M KOH	36
$NiCo_2O_4$	2.0@400	50	1.0 M KOH	37
NiFe-LDH/NiMo	1.8@370	Room temperature	1.0 M KOH	38
NiCoFe-NDA	1.8@325	50	0.1 M KOH	39
Co,Y-NiFeOOH	2.13@1000	25	1.0 M KOH	40
Ni/Co-TAPP-HNA	2.45@1000	25	1.0 M KOH	41
V-$NiFe(OOH)/Ni_3N$	1.85@685	70	1.0 M KOH	42
NiFeCu	2.3@1200	80	Pure water	43
Co, V_M-NiFe OOH	1.94@2000	Room temperature	1.0 M KOH	44
Pt_{SA}-Mn,Fe-Ni LDH	1.79@500	60	1.0 M KOH	45
CoVO@NF	1.76@500	70	1.0 M KOH	46
$NiFeS@Ti_3C_2/NF$	1.85@401	50	1.0 M KOH	47

Supplementary References

1 S. Anantharaj, M. Jayachandran and S. Kundu, *Chem. Sci.*, 2016, **7**, 3188-3205.

2 S. Anantharaj, S. R. Ede, K. Karthick, S. Sam Sankar, K. Sangeetha, P. E. Karthik and S. Kundu, *Energy Environ. Sci.*, 2018, **11**, 744-771.

3 L. Trotochaud, S. L. Young, J. K. Ranney and S. W. Boettcher, *J. Am. Chem. Soc.*, 2014, **136**, 6744-6753.

4 L. Trotochaud, J. K. Ranney, K. N. Williams and S. W. Boettcher, *J. Am. Chem. Soc.*, 2012, **134**, 17253-17261.

5 X. Jia, H. Kang, X. Yang, Y. Li, K. Cui, X. Wu, W. Qin and G. Wu, *Appl. Catal. B: Environ.*, 2022, **312**, 121389.

6 Y. Liu, X. Li, S. Zhang, Z. Wang, Q. Wang, Y. He, W.-H. Huang, Q. Sun, X. Zhong, J. Hu, X. Guo, Q. Lin, Z. Li, Y. Zhu, C.-C. Chueh, C.-L. Chen, Z. Xu and Z. Zhu, *Adv. Mater.*, 2023, **35**, 2300945.

7 Q. Niu, M. Yang, D. Luan, N. W. Li, L. Yu and X. W. Lou, *Angew. Chem. Int. Ed.*, 2022, **61**, e202213049.

8 X. Zhang, F. Yan, X. Ma, C. Zhu, Y. Wang, Y. Xie, S.-L. Chou, Y. Huang and Y. Chen, *Adv. Energy Mater.*, 2021, **11**, 2102141.

9 L. Zhong, L. He, N. Wang, Y. Chen, X. Xie, B. Sun, J. Qian, S. Komarneni and W. Hu, *Appl. Catal. B: Environ.*, 2023, **325**, 122343.

10 J. Ma, S. Wang, W. He, H. Chen, X. Zhai, F. Meng and Y. Fu, *ChemSusChem*, 2021, **14**, 5042-5048.

11 S. Li, X. Yang, S. Yang, Q. Gao, S. Zhang, X. Yu, Y. Fang, S. Yang and X. Cai, *J. Mater. Chem. A*, 2020, **8**, 5601-5611.

12 P.-F. Guo, Y. Yang, W.-J. Wang, B. Zhu, W.-T. Wang, Z.-Y. Wang, J.-L. Wang, K. Wang, Z.-H. He and Z.-T. Liu, *Chem. Eng. J.*, 2021, **426**, 130768.

13 L. Zhao, J. Yan, H. Huang, X. Du, H. Chen, X. He, W. Li, W. Fang, D. Wang, X. Zeng, J. Dong and Y. Liu, *Adv. Funct. Mater.*, 2024, **34**, 2310902.

14 S. Wakamatsu, M. S. Islam, Y. Shudo, M. Fukuda, R. Tagawa, N. Goto, M. Koinuma, Y. Sekine and S. Hayami, *Energy Adv.*, 2023, **2**, 1375-1380.

15 T. Bhowmik, M. K. Kundu and S. Barman, *ACS Appl. Energy Mater.*, 2018, **1**, 1200-

1209.

16 T. Kou, S. Wang, J. L. Hauser, M. Chen, S. R. J. Oliver, Y. Ye, J. Guo and Y. Li, *ACS Energy Lett.*, 2019, **4**, 622-628.

17 Y. Lin, H. Wang, C.-K. Peng, L. Bu, C.-L. Chiang, K. Tian, Y. Zhao, J. Zhao, Y.-G. Lin, J.-M. Lee and L. Gao, *Small*, 2020, **16**, 2002426.

18 L. Yu, J. F. Yang, B. Y. Guan, Y. Lu and X. W. Lou, *Angew. Chem. Int. Ed.*, 2018, **57**, 172-176.

19 Z. He, J. Zhang, Z. Gong, H. Lei, D. Zhou, N. Zhang, W. Mai, S. Zhao and Y. Chen, *Nat. Commun.*, 2022, **13**, 2191.

20 J. Nai, X. Xu, Q. Xie, G. Lu, Y. Wang, D. Luan, X. Tao and X. W. Lou, *Adv. Mater.*, 2022, **34**, 2104405.

21 L. Zhou, C. Zhang, Y. Zhang, Z. Li and M. Shao, *Adv. Funct. Mater.*, 2021, **31**, 2009743.

22 L. Yin, Y. Liu, S. Zhang, Y. Huang, Q. Wang, J.-C. Liu, C. Gu and Y. Du, *Mater. Horiz.*, 2025, **12**, 5400-5409.

23 R. Jiang, J. Zhang, J. Gao, Y. Xie, L. Wu, Y. Wang, Z. Xu, Z.-S. Wu, S. Yuan and G. Xu, *Small*, 2024, **20**, 2401384.

24 J. Wang, J. Yu, X. Chen, Z. Zeng, S. He, H. Liu, Z. Du and Z. Hua, *Adv. Funct. Mater.*, e12333 DOI:10.1002/adfm.202512333.

25 A. Naderi, M. Jourshabani, M. Razi Asrami and B. K. Lee, *Chem. Eng. J.*, 2024, **484**, 149111.

26 H. Guo, L. Zhang, D. Ou, Q. Liu, Z. Wu, W. Yang, Z. Fang and Q. Shi, *Small*, 2024, **20**, 2307069.

27 S. Tao, G. Zhang, B. Qian, J. Yang, S. Chu, C. Sun, D. Wu, W. Chu and L. Song, *Appl. Catal. B: Environ.*, 2023, **330**, 122600.

28 Y. Wang, N. Gong, G. Niu, J. Ge, X. Tan, M. Zhang, H. Liu, H. Wu, T. L. Meng, H. Xie, K. Hippalgaonkar, Z. Liu and Y. Huang, *J. Alloys Compd.*, 2023, **960**, 171039.

29 L. Yang, R. He, M. Botifoll, Y. Zhang, Y. Ding, C. Di, C. He, Y. Xu, L. Balcells, J. Arbiol, Y. Zhou and A. Cabot, *Adv. Mater.*, 2024, **36**, 2400572.

30 Z. Wei, M. Guo and Q. Zhang, *Appl. Catal. B: Environ.*, 2023, **322**, 122101.

31 Y. Shi, L. Song, Y. Liu, T. Wang, C. Li, J. Lai and L. Wang, *Adv. Energy Mater.*, 2024, **14**, 2402046.

32 M. H. Wang, Z. X. Lou, X. Wu, Y. Liu, J. Y. Zhao, K. Z. Sun, W. X. Li, J. Chen, H. Y. Yuan, M. Zhu, S. Dai, P. F. Liu and H. G. Yang, *Small*, 2022, **18**, 2200303.

33 S. Nagappan, H. Gurusamy, H. Minhas, A. Karmakar, S. Ravichandran, B. Pathak and S. Kundu, *Small Methods*, 2024, **9**, 2401655.

34 J. Lee, H. Jung, Y. S. Park, N. Kwon, S. Woo, N. C. S. Selvam, G. S. Han, H. S. Jung, P. J. Yoo, S. M. Choi, J. W. Han and B. Lim, *Appl. Catal. B: Environ.*, 2021, **294**, 120246.

35 A. Riaz, Z. Fusco, F. Kremer, B. Gupta, D. Zhang, C. Jagadish, H. H. Tan and S. Karuturi, *Adv. Energy Mater.*, 2023, **14**, 2303001.

36 S. Li, T. Liu, W. Zhang, M. Wang, H. Zhang, C. Qin, L. Zhang, Y. Chen, S. Jiang, D. Liu, X. Liu, H. Wang, Q. Luo, T. Ding and T. Yao, *Nat. Commun.*, 2024, **15**, 3416.

37 M. Bhushan, M. Mani, A. K. Singh, A. B. Panda and V. K. Shahi, *J. Mater. Chem. A*, 2020, **8**, 17089-17097.

38 F. Wu, F. Tian, M. Li, S. Geng, L. Qiu, L. He, L. Li, Z. Chen, Y. Yu, W. Yang and Y. Hou, *Angew. Chem. Int. Ed.*, 2025, **64**, e202413250

39 K. Yue, J. Liu, Y. Zhu, C. Xia, P. Wang, J. Zhang, Y. Kong, X. Wang, Y. Yan and B. Y. Xia, *Energy Environ. Sci.*, 2021, **14**, 6546-6553.

40 X. Lv, M. Li, H. Qin, L. Jiao, Y. Lv, H. Luo, W. Zhou and L. Guo, *Adv. Sci.*, e12638 DOI: 10.1002/advs.202512638.

41 K. Wei, Z. Liu, G. Feng, Y. Wang, S. Zhang, X. Li, M. Zhang, H. Li, J. Zhou, S. Lei and F. Gao, *Adv. Energy Mater.*, 2025, **15**, 2405366.

42 P. Thangavel, H. Lee, T.-H. Kong, S. Kwon, A. Tayyebi, J.-h. Lee, S. M. Choi and Y. Kwon, *Adv. Energy Mater.*, 2023, **13**, 2203401.

43 X. Yang, J. Liang, Q. Shi, M. J. Zachman, S. Kabir, J. Liang, J. Zhu, B. Slenker, M. Pupucevski, N. Macauley, A. J. Kropf, H. Zeng, D. Strasser, D. J. Myers, H. Xu, Z. Zeng, Y. Yan and G. Wu, *Adv. Energy Mater.*, 2024, **14**, 2400029.

44 Y. Zhao, Q. Wen, D. Huang, C. Jiao, Y. Liu, Y. Liu, J. Fang, M. Sun and L. Yu, *Adv. Energy Mater.*, 2023, **13**, 2203595.

45 K. D. Tran, T. H. Nguyen, D. T. Tran, V. A. Dinh, N. H. Kim and J. H. Lee, *ACS Nano*, 2024, **18**, 16222-16235.

46 Z. Liang, D. Shen, Y. Wei, F. Sun, Y. Xie, L. Wang and H. Fu, *Adv. Mater.*, 2024, **36**, 2408634.

47 D. Chanda, K. Kannan, J. Gautam, M. M. Meshesha, S. G. Jang, V. A. Dinh and B. L. Yang, *Appl. Catal. B: Environ.*, 2023, **321**, 122039.